Near-Unity Indistinguishability of Single Photons Emitted from Dissimilar and Independent Atomic Quantum Nodes

Félix Hoffet[1,*] Jan Lowinski,[1] Lukas Heller,[1] Auxiliadora Padrón-Brito,[1] and
Hugues de Riedmatten[1,2,†]

[1]*ICFO—Institut de Ciencies Fotoniques, The Barcelona Institute of Science and Technology*, Spain
[2]*ICREA—Institució Catalana de Recerca i Estudis Avançats*, Barcelona, 08015, Spain

Generating indistinguishable photons from independent nodes is an important challenge for the development of quantum networks. In this work, we demonstrate the generation of highly indistinguishable single photons from two dissimilar atomic quantum nodes. One node is based on a fully blockaded cold Rydberg ensemble and generates on-demand single photons. The other node is a quantum repeater node based on a Duan-Lukin-Cirac-Zoller quantum memory and emits heralded single photons after a controllable memory time that is used to synchronize the two sources. We demonstrate an indistinguishability of $94.6 \pm 5.2\%$ for a temporal window including 90% of the photons. This advancement opens new possibilities for interconnecting quantum repeater and processing nodes with high-fidelity Bell state measurement without sacrificing its efficiency.

I. INTRODUCTION

Single photons play a crucial role in quantum technologies. Since their quantum state is little affected by the transmission, they are well suited as information carriers to connect and entangle distant quantum nodes [1]. In a quantum network, these quantum nodes serve specific roles, dedicated either to information processing, communication, or sensing [2]. Consequently, they utilize various physical systems, often employing photons with differing frequencies, bandwidths, and waveforms. A major challenge is to interface these different nodes and distribute entanglement between them, despite their inherent differences. This can be achieved by interfering single photons emitted from these nodes, but a high degree of indistinguishability between the photons is required [3].

The indistinguishability η between two photons can be inferred by measuring the visibility V of a Hong-Ou-Mandel interference [4]. When two photons impinge on a beam splitter, the Hong-Ou-Mandel effect states that if they are indistinguishible, they will bunch at the output,

leading to a suppression of coincidence events relative to the distinguishable scenario. This two-photon interference is also at the heart of photonic Bell state measurements, which enable quantum teleportation and the generation of entanglement between remote systems [5].

High indistinguishabilities have been demonstrated for consecutive photons emitted from a single source, including quantum dots [6–9], single rare-earth ions [10], Rydberg ensembles [11,12], spontaneous parametric down-conversion [13,14], and single atoms in cavities [15]. However, it is important to note that these results do not guarantee that independent photons from two of these sources would be indistinguishable. Ensuring the short-term stability of photon emission is different from achieving mode matching between independent sources over long periods, the latter being a more challenging task. Recently, a handful of experiments have demonstrated two-photon interference from independent sources [16–25], sometimes allowing the generation of remote entanglement between nodes based on the same platform [26–30].

However, most of these realizations had to discard a large amount of their photon detections to keep the two-photon indistinguishability sufficiently high. This is done by selecting a temporal detection window much shorter than the photon duration. In quantum communication, this selection is detrimental as it reduces the entanglement distribution rate between the two nodes. Up to now, it is still a challenge to interface independent nodes with high indistinguishability, without discarding any photon detections.

---

*Contact author: felix.hoffet@icfo.eu
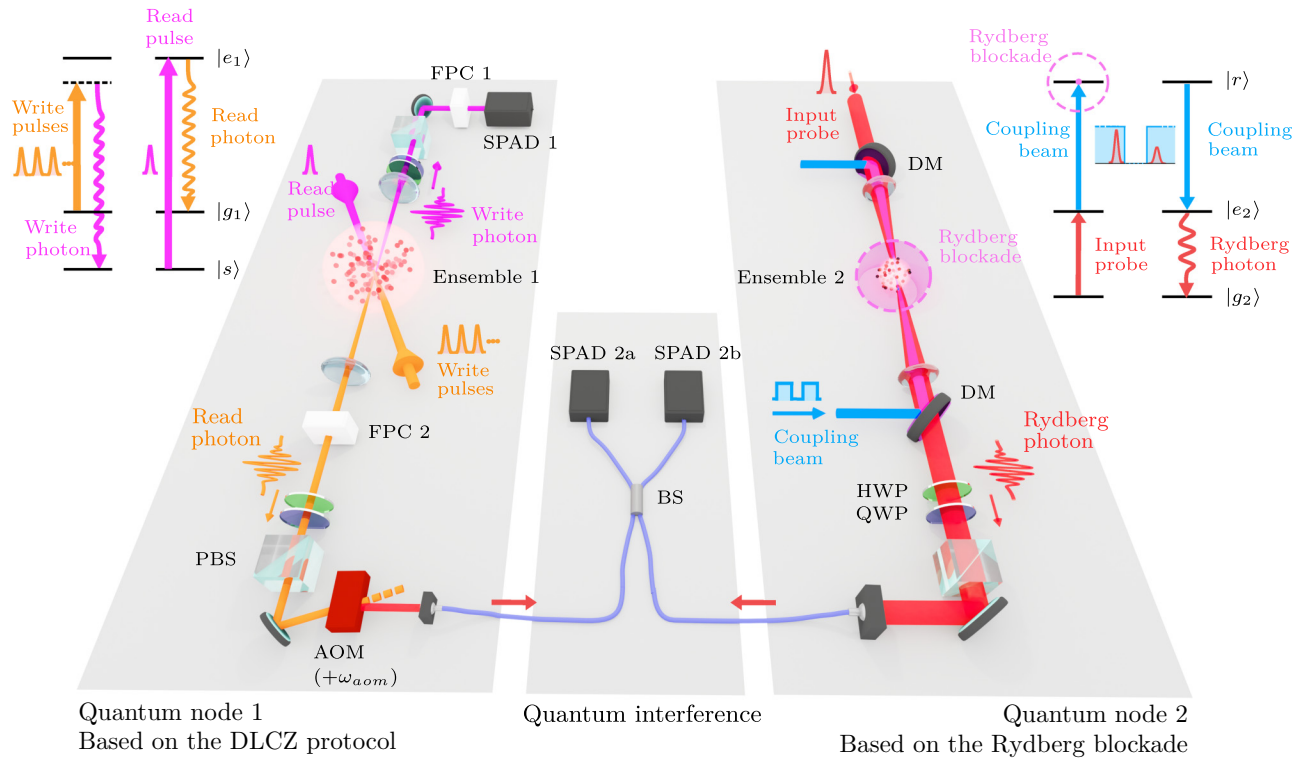†Contact author: hugues.deriedmatten@icfo.eu

FIG. 1. Schematic view of the experiment. Two quantum nodes generate independent single photons that are sent to a measurement setup, where they interfere. Quantum node 1 is based on the DLCZ protocol, where the detection of a write photon in a detector (SPAD 1) heralds a collective excitation. This excitation is later mapped to a waveshape-tunable single photon by applying a read pulse. At the same time, node 2 generates a single photon by means of dynamical Rydberg EIT in a Rydberg-blockaded ensemble. The photon generated in node 1 is frequency shifted by a single-pass acousto-optic modulator (AOM) to match that generated in node 2. Both photons are then sent to a Hong-Ou-Mandel setup consisting of two detectors [SPAD 2a(b)] and a beam splitter (BS). Coincidences are recorded in the case when both photons are set to be overlapping (indistinguishable case), and temporally separated (distinguishable case). DM, dichroic mirror; PBS, polarizing beam splitter; FPC, Fabry-Perot cavity; HWP (QWP), half- (quarter-)wave plate.

Additionally, interfacing hybrid systems adds another layer of complexity since their generated photons usually have different properties (e.g., frequencies, bandwidths, temporal modes), making them distinguishable. Hong-Ou-Mandel interferences between a single-photon source and a classical source such as a laser [31], or the Sun [32], have been demonstrated before, albeit with an overall visibility below the classical limit of 50%. To our knowledge, only one experiment measured the indistinguishability of photons emitted from dissimilar and independent matter quantum nodes [33], but again the overall interference visibility could not surpass the classical limit due to temporal-mode mismatch.

Platforms currently investigated as quantum network nodes include laser-cooled atoms and ions, as well as solid-state systems. Cold atomic ensembles provide a versatile platform that enables several functionalities. Ground-state collective excitations (spin waves) allow for the realization of long-lived and efficient quantum memories that can be used as quantum repeater nodes, using the Duan-Lukin-Cirac-Zoller (DLCZ) scheme [3,16,30,34]. Additionally,

atomic ensembles enable quantum processing nodes [35–40] and deterministic quantum light sources [11,12, 41] using the Rydberg blockade effect.

In this work, we demonstrate the generation of highly indistinguishable photons from two dissimilar cold atomic quantum nodes. Node 1 relies on the probabilistic and heralded generation of spin waves following the DLCZ protocol, later converted into a single photon after a controllable storage time used to synchronize the nodes. Triggered by node 1, node 2 then generates single photons in a deterministic fashion using Rydberg electromagnetically induced transparency [42,43], and the two photons are combined at a beam splitter. We achieve a Hong-Ou-Mandel visibility of $V = 80.2 \pm 3.6\%$, leading to an indistinguishability of $\eta = 89 \pm 4.9\%$ between the independent photons, without discarding any detection. By considering a temporal window containing 75% of the photon counts, the visibility increases to $V = 93.2 \pm 2.3\%$. This experiment opens up new possibilities for connecting remote dissimilar quantum nodes.
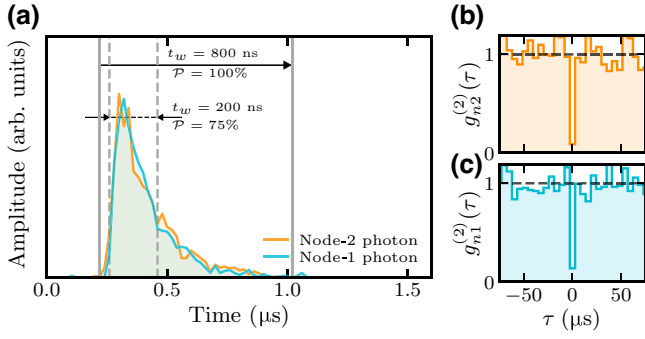
FIG. 2. Quantum node properties. (a) Temporal modes of the photons emitted from node 1 and node 2. The gray straight lines represent the temporal windows in which the coincidences of the two-photon interference experiment are counted. (b),(c) Single-photon autocorrelation of the photons emitted from node 1 and node 2. We measure $g_{n1}^{(2)}(0) = 0.13 \pm 0.04$ for the photon generated by node 1 and $g_{n2}^{(2)}(0) = 0.09 \pm 0.03$ for the photon coming out of node 2.

II. EXPERIMENTAL DETAILS

Our two quantum nodes are based on ensembles of cold ^{87}Rb atoms. They are located in the same laboratory on two optical tables separated by 3 m (see Fig. 1). We first start with the individual description of each node before we turn to the quantum interference involving their respective photons.

A. Two quantum nodes

The first node is based on the DLCZ proto-col, producing heralded photons. It has the capability to generate entangled photon pairs with an in-built quantum memory that can be used for synchronization of the network. The DLCZ protocol starts by send-ing a train of write pulses to ensemble 1, detuned by $\Delta = -40$ MHz from the $|g_1\rangle = \left|5S_{1/2}, F = 2, m_F = +2\right\rangle$ to $|e_1\rangle = \left|5P_{3/2}, F = 2, m_F = +1\right\rangle$ transition. With a low probability, this generates a write photon (Stokes photon) in the heralding mode that, upon detection at single photon avalanche detector 1 (SPAD 1), heralds a collective spin excitation in the spin state $|s\rangle = \left|5S_{1/2}, F = 1, m_F = 0\right\rangle$. After a programmable time that is set to synchronize the photon generation from two nodes (2.8 ms), we then send a read pulse resonant with the $|s\rangle \rightarrow |e_1\rangle$ transition that maps the collective excitation into a read photon (anti-Stokes photon). This photon is resonant with the $|g\rangle \rightarrow |e_1\rangle$ tran-sition and is emitted into a well-defined mode that depends on the phase-matching conditions of the process. For the DLCZ source to generate photons efficiently, the optical depth (OD) of the ensemble must be large [44,45] and the lifetime of the collective excitation must be longer than the synchronization time between the write and read

pulses. To fulfill both requirements, we employ conven-tional methods of magneto-optical trapping aided by a single retro-reflected beam dipole trap at 797 nm. This dipole trap is useful to increase the duty cycle of the exper-iment [46]. We obtain a cloud with OD = 6 and an initial temperature of about $80\,\mu$K. Furthermore, we use Fabry-Perot cavities to filter out unwanted background noise that comes from the write and read pulses, increasing both the efficiency of the heralding and the purity of the generated photons. The probability to generate a read photon condi-tioned on the detection of a write photon is around 25% with these experimental parameters. Finally, an acousto-optical modulator is employed to adjust the frequency of the read photons and to adjust the photon flux, aligning it with that of the other node.

The second node is based on a blockaded Rydberg ensemble generating single photons in a deterministic fashion. Thanks to a two-beam crossed dipole trap at 852 nm, we create a small spherical atomic cloud with a size of $13.5\,\mu$m (FWHM), OD = 12, and temperature of about $40\,\mu$K. We send a laser pulse resonant with the $|g_2\rangle = \left|5S_{1/2}, F = 2\right\rangle \rightarrow |e_2\rangle = \left|5P_{3/2}, F = 3\right\rangle$ transi-tion together with a counterpropagating coupling beam resonant with the $|e_2\rangle \rightarrow |r\rangle = \left|103S_{1/2}\right\rangle$ transition, effec-tively establishing Rydberg electromagnetically induced transparency (EIT) that creates a propagating Rydberg polariton in the cloud [42,43]. The Rydberg blockade radius is $r_b \approx 16\,\mu$m at the $n = 103$ Rydberg state [47]. Since it is larger than the cloud size, the strong dipole-dipole interactions prevent the existence of multiple Ryd-berg excitations in the cloud [48], allowing us to retrieve a single photon at the output of the cloud with a gen-eration probability of 14%. During the Rydberg polari-ton's propagation, we switch off and on the coupling field (a process known as dynamical EIT) that effectively freezes the propagation and stores the polariton in the Ryd-berg state, which is known to enhance the nonlinearity and the single photon's quality [49,50].

Because of the different natures of the two quantum nodes, their respective experimental cycles differ from one another. During the 200 ms of interrogation time of node 2, node 1 performs 17 full cycles, each one containing 4 ms of interrogation time. During each cycle, node 1 tries to herald a spin wave each 4 ms. Once a write photon is detected on SPAD 1, an electronic signal is sent to node 2 that then generates a photon that either temporally overlaps with the node-1 photon (indistinguishable case), or is sep-arated in time (distinguishable case). Every half an hour, the experiment is automatically put in calibration mode for around 10 min in order to compensate for any possi-ble slow drift. A detailed description of our experimental cycle and the communication between the two nodes is given in the Appendix A. In the distinguishable case, the final triple-coincidence rate is around 0.02 events per second.
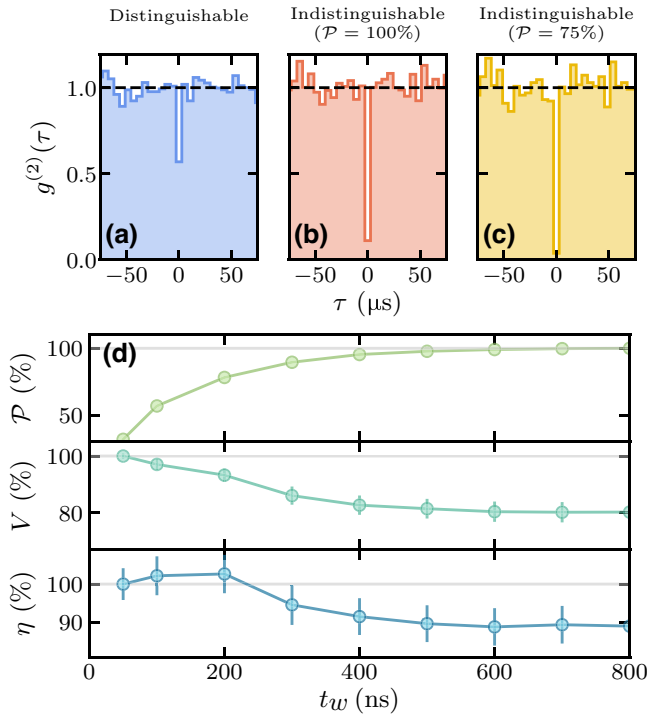
FIG. 3. Two-photon interference. (a)–(c) Normalized coincidence rate $g^{(2)}(\tau)$ between SPAD 2a and SPAD 2b in the distinguishable case (blue) and indistinguishable case for the whole pulse (red), and for a proportion $\mathcal{P} = 75\%$ of counts (yellow). (d) Measured visibility (V), indistinguishability (η), and photon count share ($\mathcal{P}$) for various lengths of the temporal window.

B. Photon mode matching

Both photons are sent to a measurement platform consisting of a fiber beam splitter (BS) and two single-photon detectors [SPAD 2a(b)]. If the two photons are completely indistinguishable, they bunch together at the output of the beam splitter and no coincidence between SPAD 2a and SPAD 2b is recorded. Truly indistinguishable photons can be obtained only if all their degrees of freedom (spatial, polarization, frequency, time) are mode matched with one another. The spatial mode matching can be ensured by using a single-mode fiber beam splitter. Since the polarization of the incoming photons needs to be well controlled at the position of the BS, we use polarization-maintaining fibers and a set of half-wave and quarter-wave plates before the fiber incoupling. Injecting classical light at slightly different frequencies into the setup and adjusting the beating fringes, we then measure a polarization matching greater than 99.9%. The frequency offset (266 MHz) determined by the atomic levels used to generate the photons in each quantum node is compensated by sending the heralded photons from the DLCZ node to a single-pass acousto-optical modulator (AOM). The temporal offset can be controlled by changing the synchronizing time (or
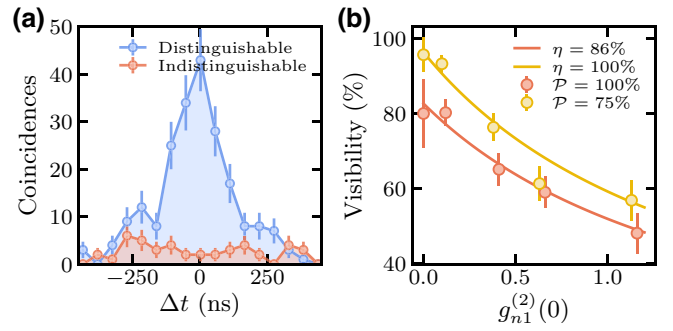

FIG. 4. (a) Number of detected coincidences separated by a time delay Δt, within the analysis window $t_{\mathrm{w}} = 800$ ns. (b) Measured two-photon visibilities for different values of the DLCZ photon autocorrelation $g_{n1}^{(2)}$ for temporal windows containing $\mathcal{P} = 100\%$ and 75% of the counts. The solid lines are the expected values estimated from Eq. (2) for indistinguishabilities of $\eta = 86\%$ (red) and $\eta = 100\%$ (yellow).

storage time) of each quantum node. Finally, assuming that both photons are Fourier limited, their frequency mode is completely determined by their temporal mode. We match the temporal mode of the DLCZ-produced photon to that of the Rydberg-produced photon by modulating the intensity of the read pulse in the DLCZ protocol [51], allowing us to maintain a temporal mode matching higher than 98%, as represented in Fig. 2(a). In both cases, we produce a photon with a steep leading edge of 60 ns and resembling an exponential decay trailing edge with $1/e$ time of around 180 ns. The photon flux is also adjusted by changing the driving amplitude of the AOM, such that the probability to have a photon at the beam splitter is similar for each source (around 2.8% per trial).

To evaluate the quality of each photon, we measure the autocorrelation functions $g_{n1}^{(2)}(\tau = 0)$ and $g_{n2}^{(2)}(\tau = 0)$. The results are displayed in Fig. 2(b), where the counts are integrated over a temporal window of length $t_{\mathrm{w}} = 800$ ns in each 5.4-μs-long bin, representing one experimental trial. We measure $g_{n1}^{(2)}(0) = 0.13 \pm 0.04$ for the photon generated by node 1 and $g_{n2}^{(2)}(0) = 0.09 \pm 0.03$ for the photon coming from node 2.

III. TWO-PHOTON INTERFERENCE

We now move to the two-photon interference between the two quantum nodes. In both the indistinguishable case and distinguishable case, we record coincidences to measure the visibility of the two-photon interference, which is given by

$$V = 1 - \frac{g_i^{(2)}(0)}{g_d^{(2)}(0)}, \qquad (1)$$

where $g_d^{(2)}(0)$ [$g_i^{(2)}(0)$] is the normalized coincidence rate between SPAD 2a and SPAD 2b in the distinguishable

(indistinguishable) case. Coincidences are recorded in a specific temporal window, as illustrated in Fig. 2 where a window of length $t_w = 800$ ns contains $\mathcal{P} = 100\%$ of the photon counts and another window of length $t_w = 200$ ns contains a proportion of $\mathcal{P} = 75\%$.

For counts integrated over the full window ($t_w = 800$ ns), we measure a visibility of $V = 80.2 \pm 3.6\%$ with $g_d^{(2)}(0) = 0.57 \pm 0.05$ and $g_i^{(2)}(0) = 0.11 \pm 0.02$, as shown in Figs. 3(a) and 3(b). This result is, to our knowledge, the highest reported visibility of a two-photon interference in hybrid systems, and it is higher than most realizations with nodes made of the same platform without discarding photon counts. If we take $\mathcal{P} = 75\%$ of all photon counts ($t_w = 200$ ns), we measure a visibility as high as $V = 93.2 \pm 2.3\%$, with $g_i^{(2)}(0) = 0.04 \pm 0.01$. We further confirm the strong suppression of the coincidence rate for overlapping pulses by looking at the time-resolved HOM interference, as shown in Fig. 4(a). When the photons are set to be distinguishable, we observe a peak of coincidences (blue data) around zero delay that is linked to the convolution of the photons' temporal modes. One can appreciate a strong suppression of the coincidence number (red data) over the whole temporal window. We emphasize here that the results presented in this paragraph were measured with raw coincidences and without correction of any kind.

To estimate the indistinguishability η between the two photons, we take into account the fact that the nonzero value of the single-photon autocorrelation $g^{(2)}(0)$ (see Fig. 2) reduces the visibility of the interference. For a 50:50 beam splitter, assuming that each node emits at most two photons, the indistinguishability η can then be evaluated using the formula [33]

$$V = \frac{2\eta}{g_{n1}^{(2)}(0)x + g_{n2}^{(2)}(0)/x + 2},\qquad(2)$$

where $g_{n1}^{(2)}(0)$ [$g_{n2}^{(2)}(0)$] is the autocorrelation of the photon incoming from node 1 (2) and $x = p_{n1}/p_{n2}$ is the ratio between the probabilities of detecting a photon from nodes 1 and 2. We infer an indistinguishability $\eta = 89.2 \pm 4.9\%$ for $\mathcal{P} = 100\%$. The indistinguishability increases to $94.6\% \pm 5.2\%$ for $\mathcal{P} = 90\%$ and becomes compatible with unity within error bars for $\mathcal{P} = 75\%$, showing that both photons exhibit a near-perfect indistinguishability between one another. To further study this interference, we repeat this measurement for different values of $g_{n1}^{(2)}(0)$ to see if the scaling of the visibility in Eq. (2) is well respected. The autocorrelation $g_{n1}^{(2)}(0)$ can be changed by varying the write pulse power in the writing stage of the DLCZ protocol, which changes the probability of generating more than one atomic excitation. These measurements are plotted in Fig. 4 alongside the predictions of Eq. (2) (solid lines) with parameters

$x = 1.3$, $g_{n2}^{(2)}(0) = 0.1$ and where the indistinguishability is $\eta = \{86\%, 100\%\}$ for $\mathcal{P} = \{100\%, 75\%\}$. We observe good agreement between our data and the formula, indicating that our visibility is indeed reduced due to nonzero two-photon suppression of each photon.

Finally, we plot in Fig. 3(d) the visibility V, indistinguishability η, and proportion $\mathcal{P}$ of photon detections as a function of the length of the temporal window t_w. In the limit of a large temporal window, we observe a saturation of indistinguishability η around 90%, meaning that the photons' mode matching is not perfect. We attribute this to a small spectral impurity, meaning that our photons might not be completely Fourier limited. By decreasing t_w, we effectively broaden our frequency mode, allowing for a better overlap in frequency space, and thus higher indistinguishabilities. For completeness, we explain here why some values of η were found to be above unity for small t_w. The estimator of Eq. (2) is bounded, in the sense that if all the relevant quantities ($g_{n1}^{(2)}(0)$, $g_{n2}^{(2)}(0)$, V, and x) were measured simultaneously, it would not be possible to obtain a value of indistinguishability larger than unity. However, in our experiment we had to measure these values separately and we were therefore exposed to statistical fluctuations. If the indistinguishability is close to unity, the probability of finding $\eta > 100\%$ is therefore high. We emphasize here that our measurements are compatible with unity within error bars, as the error bar goes down to 97%.

Throughout the experiment, the input probe mean photon number of node 2 was kept low to maintain low $g_{n2}^{(2)}(0)$. However, it is important to note that a high mean input photon number would not just degrade $g_{n2}^{(2)}(0)$, but it could also diminish the purity of the single photons generated by node 2, as predicted by Gorshkov *et al.* [52]. This decrease in purity would consequently lead to a reduction in the indistinguishability of the photons. We report on the observation of this effect and analyze our results in Appendix C.

IV. DISCUSSION AND OUTLOOK

In summary, our work demonstrates high-visibility interference of two photons produced in dissimilar and independent quantum nodes. We achieve high indistinguishability by carefully mode matching the two photons in all degrees of freedom, without the need for discarding photon detections. If this setup was used for a quantum communication protocol, such as generating remote entanglement between node 1 and node 2, the maximum achievable fidelity of the entanglement with respect to the ideal Bell state would be equal to $F = (1 - \eta)/2$ [33] for ideal single photons. Based on the data presented in Fig. 4(b), this means that, without discarding any photon detection, we would be limited to $F = 93\%$. By keeping a proportion $\mathcal{P} = 75\%$ of the counts, thus reducing the efficiency
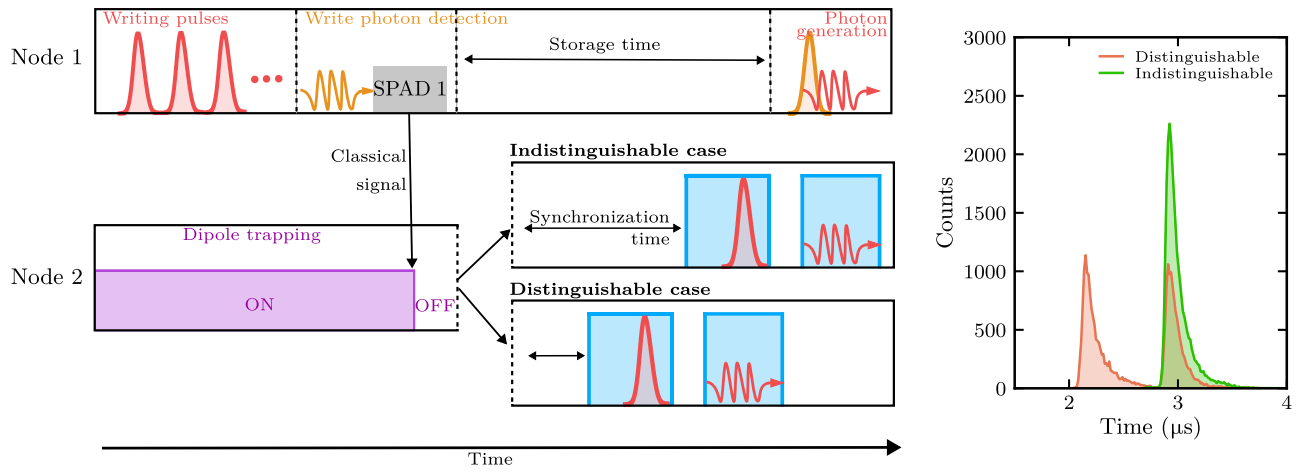
FIG. 5. Distinguishable and indistinguishable cases. Left: schematics of one experimental trial. Quantum node 2 keeps trapping atoms until it receives a classical signal from node 1, indicating that it has heralded a write photon, and will produce a read photon after 2.8 µs. After a programmable synchronization time, node 2 produces a photon using Rydberg EIT. Depending on this time, the photons emitted from node 1 and node 2 either overlap temporally (indistinguishable case) or do not (distinguishable case). Right: typical histograms obtained in the distinguishable case (red) and indistinguishable case (green).

of the protocol by only 25%, a fidelity close to $F = 100\%$ would be theoretically achievable. For such an experiment, one would need to generate entangled photon pairs in node 2, as done, for example, in Ref. [53], and perform a Bell state measurement [3]. Our setup in node 2 would need to be upgraded to gain the ability of addressing different Rydberg states at the same time and coherently control these single Rydberg excitations with high fidelity [53]. In this context, this experiment opens the path towards remote entanglement of hybrid systems, and connection of quantum processors through quantum repeater links.

APPENDIX A: NODE PROPERTIES

1. Node 1

In quantum node 1, ^{87}Rubidium atoms are trapped from background-gas pressure in a magneto-optical trap

(MOT) during 8 ms. Subsequently, the cloud is cooled by polarization-gradient cooling for 500 µs, while ramping down the magnetic field. Atoms are then prepared in the ground state $|g_1\rangle$ by Zeeman optical pumping, achieving an initial optical depth of OD = 6 on the $|g_1\rangle \rightarrow |e_1\rangle$ transition. To reduce atom loss by diffusion and a fall in gravity, the atoms are loaded into an optical dipole trap that intersects with the ensemble. The dipole trap consists of a focused light beam of linear polarization, at 796.5 nm. We focus 250 mW of power down to a beam waist of 110 µm. The light is retroreflected, forming a one-dimensional lattice with a potential depth of $U_0 \approx 400$ µK, incident at an angle of about $10°$ with the photon mode. Only then starts the interrogation time, where the write photon generation starts by sending a train of write pulses. An unsuccessful attempt is followed by a cleaning pulse, pumping the atoms back to $|g_1\rangle$. A successful heralding is instead followed by an electronic trigger sent to quantum node 2, signaling the successful generation of a spin wave. At 2.8 µs after the write pulse, a readout pulse retrieves the excitation as a photon. The $1/e^2$ beam radius is 69 µm for the photon mode and 180 µm for the excitation pulses. After 4 ms of interrogation time, the magnetic field is switched on again and the sequence repeats. The total cycle lasts about 12 ms.

The frequency of the photon is, however, not compatible with the photon produced in node 2, so it is shifted by +266 MHz with an acousto-optic modulator to make it resonant to the $|g_2\rangle \rightarrow |e_2\rangle$ transition.

2. Node 2

In quantum node 2, ^{87}Rubidium atoms are loaded in a crossed dipole trap from a MOT. We load a MOT during 1 s, followed by a temporal dark-spot compression to
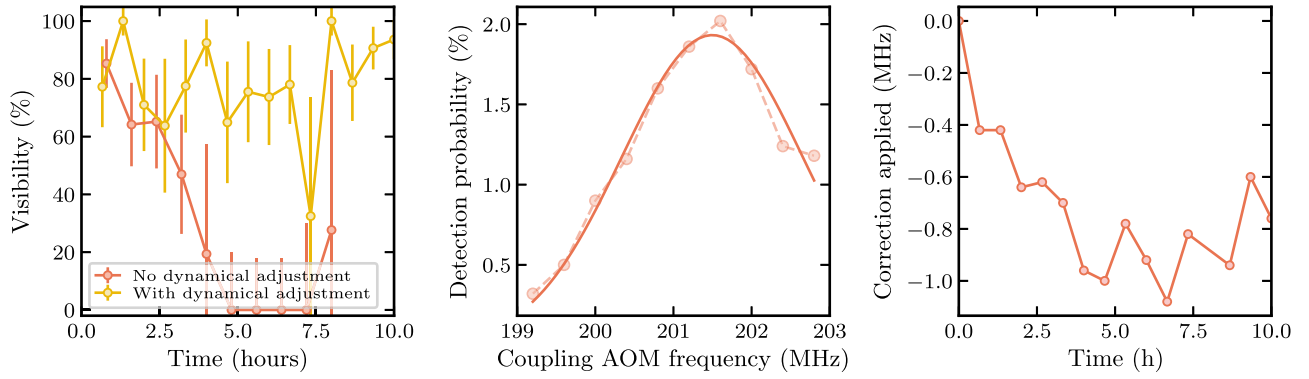
FIG. 6. Frequency stabilization in node 2. Left: two-photon interference visibility as a function of the measurement time. The experiment drifts after a few hours (red data). To counteract these drifts, we dynamically adjust the coupling beam frequency, as described in the text. The stability is greatly improved, as represented in yellow (corresponding to the data presented in the main text). Middle: by scanning the coupling frequency, we are able to find the Rydberg-EIT resonance. This measurement is performed every half hour, and the frequency is readjusted accordingly. The solid line is a Gaussian fit to the data. Right: example of the applied correction on the frequency of the coupling laser to cancel the drift of the resonance. In this case, the correction corresponds to the yellow data of the left plot.

increase the atomic density, in which the magnetic field gradient is ramped up from 20 to 50 G/cm during 9 ms. The atoms are then cooled with polarization-gradient cooling to approximately $40 \, \mu K$ for 8 ms and prepared in the ground state $|g_2\rangle$. The dipole trap consists of two tightly focused light beams of linear polarization at 852 nm, each with a power of 1 W and a beam waist of $34 \, \mu m$. One beam is horizontal, in plane with the coupling beam and photon modes, and intersects with the photon mode at an angle of $22°$. The second beam is incident from the top. This way, a spherical cloud with OD = 12 on the $|g_2\rangle \rightarrow |e_2\rangle$ transition is obtained, with a diameter of $13 \, \mu m$ (FWHM). The EIT coupling field is counterpropagating and resonant with the $|e_2\rangle \rightarrow |r\rangle$ transition, corresponding to a wavelength of 479.3118 nm, derived from a 479-nm frequency-converted amplified diode laser with a seed at 958 nm. The $1/e^2$ beam radius is $6.5 \, \mu m$ for the probe and $13.5 \, \mu m$ for the coupling mode. The total interrogation time is 200 ms, in a cycle that lasts about 1.25 s.

Depending on the measurement, we time the probe and coupling field with respect to the classical signal sent by node 1 to either overlap the generated photon with the node-1 photon or separate it in time. We call these two cases "indistinguishable" and "distinguishable," as presented in Fig. 5.

APPENDIX B: FREQUENCY STABILIZATION

Reducing the linewidths and maintaining good stability of all laser frequencies used in each quantum node is important in our experiment. This is because the visibility of the two-photon interference is sensitive to the frequency offset between each photon, which can be affected by various frequency drifts. In this appendix, we start by describing our locking systems in node 1 and in node 2.

We then discuss several instability problems that appeared in node 2, and we finally explain the method we implemented to fix them, in order to acquire a good stability over several hours of measurements. Data for the stabilization improvement is presented in Fig. 6.

In node 2, we use a cascaded lock of two main elements: modulation transfer spectroscopy (MTS) [54] and a transfer cavity. We lock our probe laser at 780 nm to the MTS signal using a method described in Ref. [55]. Careful alignment of the MTS setup allowed us to reduce frequency drifts to below 20 kHz (limited by residual amplitude modulation introduced by an electro-optic modulator). A fraction of the same laser light is sent to a 25-cm-long plano-concave transfer cavity of finesse about 1800, whose length is controlled by a mirror fixed to a piezo actuator. The cavity length is stabilized with the standard Pound-Drever-Hall (PDH) technique [56]. A small portion of the coupling laser seed light at 958 nm is sent to the same transfer cavity and its frequency is also locked with the PDH technique. This allows for not only stabilization of the central frequency, but also narrowing of the laser linewidth to about 60 kHz, as estimated by comparing the root mean square of the error signal and its slope. In node 1, one laser at 780 nm is locked to a saturated absorption spectroscopy signal offering stability of the order of 200 kHz, used for the writing pulses and magneto-optic trapping of the atoms. Another laser at 780 nm, used for reading out the collective excitation, is locked with a phase-lock-loop technique to the probe laser of node 2, reducing uncorrelated drifts between the two nodes.

In the context of high visibility of photon-photon interference, we were affected by a slow drift of the Rydberg resonance and of the coupling laser frequency in node 2, attributed to several reasons. When locked for several hours, the coupling laser residual amplitude modulation

causes a slow frequency drift, effectively changing the frequency of the node-2 photons. Additionally, the node-2 photon frequency was affected by a shift of the Rydberg-EIT resonance over the course of hours, possibly due to slow changes of the ambient electric field. The level $103S_{1/2}$ is indeed highly sensitive to an electric field, and we estimate (using the ARC package [57]) that a change in the electric field strength as small as $10\,\text{mV}\,\text{cm}^{-1}$ is enough to shift the energy level by about 1 MHz. Last, we observed that the trigger rate of the Rydberg node affects the value of the EIT resonance, if the rate is too low. This means that the resonant frequency depends on the rate of write photon detections in node 1. We do not have a clear explanation why this happens, but we understand that it is linked to the total time in which the coupling laser is shone onto the atoms, and we suspect a technical issue.

Since our experiment required performing measurements for several tens of hours, we implemented fixes in the experimental sequence to keep the resonance stable. Regarding the trigger rate issue, we understood that the resonance was affected by the amount of time the blue power was turned on during the interrogation time. To overcome this effect, we decided to turn on the coupling laser for 10 ms before the start of the interrogation time, allowing us to go out of the range at which the trigger rate influences the resonance. This fixed most of the visibility decay with measurement time. Then, to correct for both frequency drift of the coupling laser and EIT resonance drift, we implemented a dynamical method that probes the atomic resonance and readjusts the laser every half an hour to keep the coupling laser on two-photon resonance. This method consists in storing weak pulses of probe light in the Rydberg ensemble using Rydberg EIT. We then scan the coupling light frequency and find the resonance by finding the maximum of the storage efficiency. The Hong-Ou-Mandel experiment between the two nodes then starts again with the corrected coupling frequency, until another calibration is done half an hour later. The results for such a calibration sequence are presented in Fig. 6.

APPENDIX C: OBSERVATION OF DISSIPATIVE INTERACTIONS IN THE RYDBERG NODE

Theoretical predictions by Gorshkov and collaborators [52] suggested that photons generated under Rydberg-EIT conditions with a high mean number of input probe photons would be in a mixed state. This results from the fact that blockaded ensembles allow only one Rydberg excitation at a time. This means that, under perfect Rydberg-EIT conditions, only the initial photon propagates as a polariton, while subsequent ones scatter away. These scattering events occur within a distance approximately equal to the blockade radius, defined as the point where the interaction strength matches the single-atom EIT linewidth, and

is typically given by [35]

$$r_b = \sqrt[6]{\frac{C_6\Gamma}{\Omega_c^2}}, \qquad (C1)$$

where C_6 is the van der Waals coefficient (controlling interaction strength), Ω_c is the coupling Rabi frequency, and Γ is the decay rate of the excited state. Both the van der Waals coefficient and the coupling Rabi frequency scale with n, i.e., $C_6 \propto n^{11}$ and $\Omega_c \propto n^{-3/2}$.

As photons scatter at positions determined by the polariton, they carry information about its location. Therefore, each scattering event decreases the purity of the polaritonic state and, consequently, of the retrieved photonic state. Put differently, the scattered photons become entangled with the polariton, and tracing them out from the description leaves the polariton in a mixed state. The expected outcome is a reduction in the photon's purity with an increase in the mean number of input photons. Moreover, this phenomenon is associated with the spatial localization of the Rydberg polariton, where successive scattering events pinpoint the polariton's position within the cloud. This localization in space broadens the polariton in frequency, potentially causing additional absorption if it surpasses the EIT linewidth [58]. Consequently, we anticipate a decreased generation probability for larger input mean photon numbers.

We can study the reduction of the purity of the Rydberg photons owing to the fact that the visibility of the HOM interference depends on the purity of the input photon states. For perfectly separable single photons with identical spectral amplitudes [60], the HOM visibility is expressed as $V = \text{Tr}(\rho_{n1}\rho_{n2})$ [61]. Here, ρ_{n1} and ρ_{n2} refer to the density matrices of the interfering photons, while Tr signifies the matrix trace. As our photons are not perfect and exhibit a $g^{(2)}(0)$ above zero, one can equate this visibility with the indistinguishability η discussed in the main text. Since we observe η to be close to one, this suggests that $\rho_{n1} \approx \rho_{n2}$. Consequently, any alteration of ρ_{n2} will reduce the indistinguishability, specifically a reduction of its purity $\text{Tr}(\rho_{n2}^2)$.

The measurements revealing purity reduction of the Rydberg photons, as described above, are presented in Fig. 7. We observe a general trend of decreasing indistinguishability η for increasing input probe mean photon number. When we change the Rydberg level from $103S_{1/2}$ (turquoise squares) to $89S_{1/2}$ (red circles), keeping the same coupling power [62], and consequently reducing the Rydberg blockade radius r_b from 15.5 to 11 μm, which is less than the ensemble size, we observe a significantly weaker decay of the indistinguishability with input probe mean photon number. This is an expected behavior—for a fixed input probe mean photon number, if the Rydberg blockade radius is decreased below the ensemble size, the
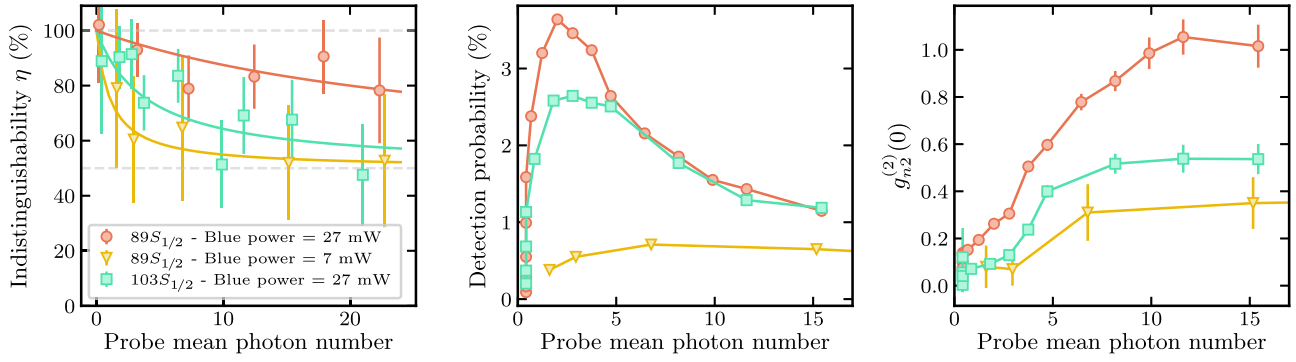
FIG. 7.   Dissipative interactions in the Rydberg node. Left: indistinguishability η of the two-photon interference for different input probe mean photon numbers in node 2, measured for different conditions of the Rydberg blockade radius by changing the Rydberg level or the EIT linewidth. We observe a decrease of η for increasing probe mean photon number, a sign of reduced purity of the generated photon due to dissipative interactions in the Rydberg medium. The solid lines are a guide to the eye, based on the purity formula proposed in Ref. [52], where we weighed the mean input photon number of each curve differently. The weights are free fitting parameters, and we did not find any meaningful relation between the weights and the blockade radii. Middle: Rydberg photon detection probability as a function of the input mean photon number. Above a few photons per pulse, the generation probability decreases, possibly due to the EIT filtering effect [58] and pollutants [59]. Right: variation of the antibunching $g_{n2}^{(2)}(0)$ of the generated photon with respect to the input probe mean photon number. For a higher blockade radius, we obtain lower values of $g_{n2}^{(2)}(0)$. The data presented in the left panel was taken with a lower optical depth and lower maximum available coupling power than the data taken for the middle and right panels. This is because these measurements were performed at different times, when experimental conditions were different.

number of scattering events is reduced and the purity of the photonic state is higher [at the expense of increased $g^{(2)}(0)$]. We then again increase the blockade radius to 13 µm by reducing the coupling Rabi frequency at $89S_{1/2}$ (yellow triangles), and observe a stronger decay of η. We do not know the reason why this decay is stronger than in the 15.5-µm case.

These results constitute the observation of the effects predicted in Ref. [52]. Nevertheless, notable disparities exist between the theory and our experiment. Gorshkov *et al.* [52] assumed that the pulses were fully compressed within the medium, a condition not met in our experiment. However, by performing the storage we effectively discard parts of the pulse that were not affected by the blockade effect, bringing it closer to the theory conditions. At the same time, the storage is known to enhance the Rydberg medium nonlinearity [41,49], deviating our experiment from the theory consideration.

Moreover, limitations of our experimental data hinder definitive conclusions. First, our results exhibit large error bars for large input mean photon numbers and low Ω_c, limited by a low generation probability, as pictured in the middle panel of Fig. 7, possibly due to the EIT filtering effect as described earlier and so-called pollutants [59]. Additionally, even though we kept the same DLCZ excitation probability in node 1 for this measurement, we had to adapt the read pulse waveform since the photons produced with smaller Ω_c in the Rydberg medium have a longer wave shape. This might also have changed the properties of node 1's photons for each configuration in this measurement.

APPENDIX D: HONG-OU-MANDEL DIP

To further explore the properties of our photon-photon interference, we measure a Hong-Ou-Mandel dip in the frequency domain as plotted in Fig. 8. We scan the frequency difference of the two photons by changing the frequency of the AOM of node 1. We observe a dip resembling a Lorentzian shape, as expected for photons having an exponential temporal waveform. Depending on the length of the temporal window used for analysis, the FWHM of the dip is modified, a nice example that
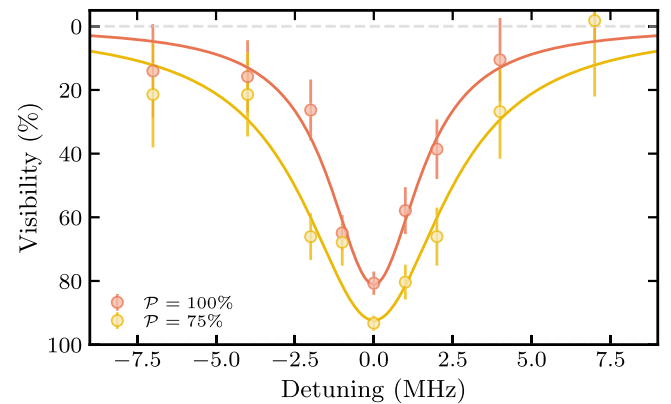

FIG. 8.   Hong-Ou-Mandel dip in frequency space. The frequency of the AOM is varied to change the detuning between the two photons. The FWHM of the dip is larger for the temporal window containing a smaller proportion $\mathcal{P}$ of the counts. Solid lines are Lorentzian fits to the data, as expected for exponential photons.

shows that reducing the temporal-window is equivalent to artificially increasing the bandwidth of the photons, thus increasing the overlap of their modes.

APPENDIX E: VISIBILITY CALCULATION

We explain here our choice to evaluate the visibility of the two-photon interference with the normalized coincidence probability in the case where the photons are distinguishable [$g_d^{(2)}(0)$] compared to the case in which they are indistinguishable [$g_i^{(2)}(0)$], following

$$V = 1 - \frac{g_i^{(2)}(0)}{g_d^{(2)}(0)}, \tag{E1}$$

which is Eq. (1) in the main text. We argue that this approach is more conservative and more reliable compared to estimating visibility through direct comparison of raw coincidences in distinguishable and indistinguishable cases, a common practice in many studies.

For both methods of calculating the visibility, it is necessary to measure independently distinguishable and indistinguishable cases. This makes the results susceptible to experimental drifts, such as fluctuations in photon generation efficiency or optical losses over the extended experimental time. For instance, if the photon generation rate dropped during indistinguishable coincidence measurements compared to distinguishable ones, the visibility would be erroneously higher. By utilizing normalized coincidence probabilities, these types of fluctuations are effectively mitigated. It is important to note that, while this method enhances reliability, it does not eliminate the inherent statistical uncertainties of our measurements and the effect of other types of experimental drift that might also affect the result.

In the following calculation, we explain how we obtain Eq. (2) of the main text. We start by estimating the probability $\mathcal{P}$ of having one photon at each output port of the BS per experimental trial. For a 50:50 BS,

$$\mathcal{P} = p_1^{(n1)} p_1^{(n2)} (1 - P_{\text{HOM}}) + \tfrac{1}{2} p_2^{(n1)} + \tfrac{1}{2} p_2^{(n2)}, \tag{E2}$$

where $p_1^{(n1)}$ ($p_1^{(n2)}$) is the probability that a single photon from node 1 (node 2) arrives at the BS, $p_2^{(n1)}$ ($p_2^{(n2)}$) is the probability that two photons from node 1 (node 2) arrive at the BS, and P_{HOM} is the probability that the single photons emitted from node 1 and node 2 bunch when they arrive at the BS. The terms containing $p_2^{(n1)}$ and $p_2^{(n2)}$ are multiplied by 1/2, since the probability that two photons impinging on the BS exit with one photon at each port is equal to 1/2. We neglect higher-order processes. It can be shown (for

example, in the supplementary material of Ref. [33]) that

$$P_{\text{HOM}} = \frac{1 + \eta}{2}, \tag{E3}$$

where η is the mode overlap (the indistinguishability) of the photons. Factoring $p_1^{(n1)} p_1^{(n2)}$ out of Eq. (E2), we get

$$\mathcal{P} = p_1^{(n1)} p_1^{(n2)} \left[\frac{1 - \eta}{2} + \frac{1}{2} \frac{p_2^{(n1)}}{p_1^{(n1)} p_1^{(n2)}} + \frac{1}{2} \frac{p_2^{(n2)}}{p_1^{(n1)} p_1^{(n2)}} \right]. \tag{E4}$$

We identify that

$$g_{n1}^{(2)}(0) \approx \frac{2 p_2^{(n1)}}{p_1^{(n1)} p_1^{(n1)}} \quad \text{and} \quad g_{n2}^{(2)}(0) \approx \frac{2 p_2^{(n2)}}{p_1^{(n2)} p_1^{(n2)}}, \tag{E5}$$

and using the notation $x = p_1^{(n1)}/p_1^{(n2)}$, we arrive at

$$\mathcal{P} = p_1^{(n1)} p_1^{(n2)} \left[\frac{1 - \eta}{2} + \frac{1}{4} g_{n1}^{(2)}(0) x + \frac{1}{4} g_{n2}^{(2)}(0) \frac{1}{x} \right]. \tag{E6}$$

We can now express the normalized detected coincidence probabilities as the ratio of having a coincidence click divided by the product of the probabilities of having a single click in detector 2a and detector 2b. When photons are completely distinguishable, $\eta = 0$ and we have

$$g_d^{(2)}(0) = \frac{\mathcal{P}|_{\eta=0} \, \alpha_{2a} \alpha_{2b}}{\left[(p_1^{(n1)}/2 + p_1^{(n2)}/2) \alpha_{2a} \, (p_1^{(n1)}/2 + p_1^{(n2)}/2) \alpha_{2b} \right]}$$
$$= \frac{4x}{(1 + x)^2} \left[\frac{1}{2} + \frac{1}{4} g_{n1}^{(2)}(0) x + \frac{1}{4} g_{n2}^{(2)}(0) \frac{1}{x} \right], \tag{E7}$$

where α_{2a} (α_{2b}) is the detection efficiency of detector 2a (2b) in Fig. 1. Similarly, in the indistinguishable case, we can write

$$g_i^{(2)}(0) = \frac{4x}{(1 + x)^2} \left[\frac{1 - \eta}{2} + \frac{1}{4} g_{n1}^{(2)}(0) x + \frac{1}{4} g_{n2}^{(2)}(0) \frac{1}{x} \right]. \tag{E8}$$

We note that these quantities are dependent on $p_1^{(n1)}$ and $p_1^{(n2)}$ only through their ratio x and the autocorrelations $g_{n1}^{(2)}$ and $g_{n2}^{(2)}$. This means that if there is a global change in the detection rate, it does not affect the visibility, which is why this approach is more robust, as explained at the beginning of this appendix. Finally, assuming that x, $g_{n1}^{(2)}$, and $g_{n2}^{(2)}$ are constant during both measurements of $g_d^{(2)}(0)$ and $g_i^{(2)}(0)$, we insert the last two equations into Eq. (E1) to

obtain Eq. (2) of the main text:

$$V = \frac{2\eta}{g_{n1}^{(2)}(0)x + g_{n2}^{(2)}(0)/x + 2}. \qquad \text{(E9)}$$

[1] H. J. Kimble, The quantum internet, Nature **453**, 1023 (2008).

[2] S. Wehner, D. Elkouss, and R. Hanson, Quantum internet: A vision for the road ahead, Science **362**, 8 (2018).

[3] N. Sangouard, C. Simon, H. de Riedmatten, and N. Gisin, Quantum repeaters based on atomic ensembles and linear optics, Rev. Mod. Phys. **83**, 33 (2011).

[4] C. K. Hong, Z. Y. Ou, and L. Mandel, Measurement of subpicosecond time intervals between two photons by interference, Phys. Rev. Lett. **59**, 2044 (1987).

[5] S. Pirandola, J. Eisert, C. Weedbrook, A. Furusawa, and S. L. Braunstein, Advances in quantum teleportation, Nat. Photonics **9**, 641 (2015).

[6] X. Ding, Y. He, Z.-C. Duan, N. Gregersen, M.-C. Chen, S. Unsleber, S. Maier, C. Schneider, M. Kamp, S. Höfling, C.-Y. Lu, and J.-W. Pan, On-demand single photons with high extraction efficiency and near-unity indistinguishability from a resonantly driven quantum dot in a micropillar, Phys. Rev. Lett. **116**, 020401 (2016).

[7] D. Cogan, Z.-E. Su, O. Kenneth, and D. Gershoni, Deterministic generation of indistinguishable photons in a cluster state, Nat. Photonics **17**, 324 (2023).

[8] D. Huber, M. Reindl, Y. Huo, H. Huang, J. S. Wildmann, O. G. Schmidt, A. Rastelli, and R. Trotta, Highly indistinguishable and strongly entangled photons from symmetric GaAs quantum dots, Nat. Commun. **8**, 15506 (2017).

[9] N. Coste, D. A. Fioretto, N. Belabas, S. C. Wein, P. Hilaire, R. Frantzeskakis, M. Gundin, B. Goes, N. Somaschi, M. Morassi, A. Lemaître, I. Sagnes, A. Harouri, S. E. Economou, A. Auffeves, O. Krebs, L. Lanco, and P. Senellart, High-rate entanglement between a semiconductor spin and indistinguishable photons, Nat. Photon. **17**, 582 (2023).

[10] S. Ourari, L. Dusanowski, S. P. Horvath, M. T. Uysal, C. M. Phenicie, P. Stevenson, M. Raha, S. Chen, R. J. Cava, and J. D. Thompson, Indistinguishable telecom band photons from a single Er ion in the solid state, Nature **620**, 977 (2023).

[11] D. P. Ornelas-Huerta, A. N. Craddock, E. A. Goldschmidt, A. J. Hachtel, Y. Wang, P. Bienias, A. V. Gorshkov, S. L. Rolston, and J. V. Porto, On-demand indistinguishable single photons from an efficient and pure source based on a Rydberg ensemble, Optica **7**, 813 (2020).

[12] S. Shi, B. Xu, K. Zhang, G.-S. Ye, D.-S. Xiang, Y. Liu, J. Wang, D. Su, and L. Li, High-fidelity photonic quantum logic gate based on near-optimal Rydberg single-photon source, Nat. Commun. **13**, 4454 (2022).

[13] N. Bruno, A. Martin, T. Guerreiro, B. Sanguinetti, and R. T. Thew, Pulsed source of spectrally uncorrelated and indistinguishable photons at telecom wavelengths, Opt. Express **22**, 17246 (2014).

[14] C. Xiong, X. Zhang, Z. Liu, M. J. Collins, A. Mahendra, L. G. Helt, M. J. Steel, D.-Y. Choi, C. J. Chae, P. H. W. Leong, and B. J. Eggleton, Active temporal multiplexing of indistinguishable heralded single photons, Nat. Commun. **7**, 10853 (2016).

[15] P. B. R. Nisbet-Jones, J. Dilley, D. Ljunggren, and A. Kuhn, Highly efficient source for indistinguishable single photons of controlled shape, New J. Phys. **13**, 103036 (2011).

[16] D. Felinto, C. W. Chou, J. Laurat, E. W. Schomburg, H. de Riedmatten, and H. J. Kimble, Conditional control of the quantum states of remote atomic memories for quantum networking, Nat. Phys. **2**, 844 (2006).

[17] A. Sipahigil, K. D. Jahnke, L. J. Rogers, T. Teraji, J. Isoya, A. S. Zibrov, F. Jelezko, and M. D. Lukin, Indistinguishable photons from separated silicon-vacancy centers in diamond, Phys. Rev. Lett. **113**, 113602 (2014).

[18] F. Samara, N. Maring, A. Martin, A. S. Raja, T. J. Kippenberg, H. Zbinden, and R. Thew, Entanglement swapping between independent and asynchronous integrated photon-pair sources, Quantum Sci. Technol. **6**, 045024 (2021).

[19] Z. X. Koong, M. Cygorek, E. Scerri, T. S. Santana, S. I. Park, J. D. Song, E. M. Gauger, and B. D. Gerardot, Coherence in cooperative photon emission from indistinguishable quantum emitters, Sci. Adv. **8**, eabm8171 (2022).

[20] X. You, et al., Quantum interference with independent single-photon sources over 300 km fiber, Adv. Photonics **4**, 066003 (2022).

[21] R. Waltrich, M. Klotz, V. Agafonov, and A. Kubanek, Two-photon interference from silicon-vacancy centers in remote nanodiamonds, ArXiv:2306.10524.

[22] A. Stolk, K. van der Enden, M.-C. Roehsner, A. Teepe, S. Faes, C. Bradley, S. Cadot, J. van Rantwijk, I. te Raa, R. Hagen, A. Verlaan, J. Biemond, A. Khorev, R. Vollmer, M. Markham, A. Edmonds, J. Morits, T. Taminiau, E. van Zwet, and R. Hanson, Telecom-band quantum interference of frequency-converted photons from remote detuned NV centers, PRX Quantum **3**, 020359 (2022).

[23] R. Duquennoy, M. Colautti, R. Emadi, P. Majumder, P. Lombardi, and C. Toninelli, Real-time two-photon interference from distinct molecules on the same chip, Optica **9**, 731 (2022).

[24] L. Zhai, G. N. Nguyen, C. Spinnler, J. Ritzmann, M. C. Löbl, A. D. Wieck, A. Ludwig, A. Javadi, and R. J. Warburton, Quantum interference of identical photons from remote GaAs quantum dots, Nat. Nanotechnol. **17**, 829 (2022).

[25] C.-N. Zhang, H. Li, J.-P. Dou, F. Lu, H.-Z. Yang, X.-L. Pang, and X.-M. Jin, Hong-Ou-Mandel interference linking independent room-temperature quantum memories, Photon. Res. **10**, 2388 (2022).

[26] C. W. Chou, H. de Riedmatten, D. Felinto, S. V. Polyakov, S. J. van Enk, and H. J. Kimble, Measurement-induced entanglement for excitation stored in remote atomic ensembles, Nature **438**, 828 (2005).

[27] V. Krutyanskiy, M. Galli, V. Krcmarsky, S. Baier, D. A. Fioretto, Y. Pu, A. Mazloom, P. Sekatski, M. Canteri, M. Teller, J. Schupp, J. Bate, M. Meraner, N. Sangouard, B. P. Lanyon, and T. E. Northup, Entanglement of trapped-ion qubits separated by 230 m, Phys. Rev. Lett. **130**, 050803 (2023).

[28] T. van Leent, M. Bock, F. Fertig, R. Garthoff, S. Eppelt, Y. Zhou, P. Malik, M. Seubert, T. Bauer, W. Rosenfeld, W. Zhang, C. Becher, and H. Weinfurter, Entangling single atoms over 33 km telecom fibre, Nature **607**, 69 (2022).

[29] W. Zhang, T. van Leent, K. Redeker, R. Garthoff, R. Schwonnek, F. Fertig, S. Eppelt, W. Rosenfeld, V. Scarani, C. C.-W. Lim, and H. Weinfurter, A device-independent quantum key distribution system for distant users, Nature **607,** 687 (2022).

[30] Y. Yu, F. Ma, X.-Y. Luo, B. Jing, P.-F. Sun, R.-Z. Fang, C.-W. Yang, H. Liu, M.-Y. Zheng, X.-P. Xie, W.-J. Zhang, L.-X. You, Z. Wang, T.-Y. Chen, Q. Zhang, X.-H. Bao, and J.-W. Pan, Entanglement of two quantum memories via fibres over dozens of kilometres, Nature **578,** 240 (2020).

[31] A. J. Bennett, R. B. Patel, C. A. Nicoll, D. A. Ritchie, and A. J. Shields, Interference of dissimilar photon sources, Nat. Phys. **5,** 715 (2009).

[32] Y.-H. Deng, *et al.*, Quantum interference between light sources separated by 150 million kilometers, Phys. Rev. Lett. **123,** 080401 (2019).

[33] A. N. Craddock, J. Hannegan, D. P. Ornelas-Huerta, J. D. Siverns, A. J. Hachtel, E. A. Goldschmidt, J. V. Porto, Q. Quraishi, and S. L. Rolston, Quantum interference between photons from an atomic ensemble and a remote atomic ion, Phys. Rev. Lett. **123,** 213601 (2019).

[34] L.-M. Duan, M. D. Lukin, J. I. Cirac, and P. Zoller, Long-distance quantum communication with atomic ensembles and linear optics, Nature **414,** 413 (2001).

[35] O. Firstenberg, C. S. Adams, and S. Hofferberth, Nonlinear quantum optics mediated by Rydberg interactions, J. Phys. B: At., Mol. Opt. Phys. **49,** 152003 (2016).

[36] D. Paredes-Barato and C. S. Adams, All-optical quantum information processing using Rydberg gates, Phys. Rev. Lett. **112,** 040501 (2014).

[37] C. S. Adams, J. D. Pritchard, and J. P. Shaffer, Rydberg atom quantum technologies, J. Phys. B: At., Mol. Opt. Phys. **53,** 012002 (2019).

[38] H. Busche, P. Huillery, S. W. Ball, T. Ilieva, M. P. A. Jones, and C. S. Adams, Contactless nonlinear optics mediated by long-range Rydberg interactions, Nat. Phys. **13,** 655 (2017).

[39] D. Tiarks, S. Schmidt-Eberle, T. Stolz, G. Rempe, and S. Dürr, A photon–photon quantum gate based on Rydberg interactions, Nat. Phys. **15,** 124 (2019).

[40] T. Stolz, H. Hegels, M. Winter, B. Röhr, Y.-F. Hsiao, L. Husel, G. Rempe, and S. Dürr, Quantum-logic gate between two optical photons with an average efficiency above 40%, Phys. Rev. X **12,** 021035 (2022).

[41] J. Lowinski, L. Heller, F. Hoffet, A. Padrón-Brito, K. Theophilo, and H. de Riedmatten, Strongly nonlinear interaction between nonclassical light and a blockaded Rydberg atomic ensemble, Phys. Rev. Lett. **132,** 053001 (2024).

[42] J. D. Pritchard, D. Maxwell, A. Gauguet, K. J. Weatherill, M. P. A. Jones, and C. S. Adams, Cooperative atom-light interaction in a blockaded Rydberg ensemble, Phys. Rev. Lett. **105,** 193603 (2010).

[43] D. Petrosyan, J. Otterbach, and M. Fleischhauer, Electromagnetically induced transparency with Rydberg atoms, Phys. Rev. Lett. **107,** 213601 (2011).

[44] J. Simon, H. Tanji, J. K. Thompson, and V. Vuletić, Interfacing collective atomic excitations and single photons, Phys. Rev. Lett. **98,** 183601 (2007).

[45] Nevertheless, OD should not be too large since it can lead to incoherent absorption and reduction of efficiency.

[46] However, the increase in the duty cycle is partial, since the writing process of the DLCZ protocol heats the atoms and is associated with rapid loss of optical depth. Still, when producing photons with low $g_{n1}^{(2)}(0)$, we were able to keep a sufficient optical depth during the 4 ms of interrogation time.

[47] S. Weber, C. Tresp, H. Menke, A. Urvoy, O. Firstenberg, H. P. Büchler, and S. Hofferberth, Calculation of Rydberg interaction potentials, J. Phys. B: At., Mol. Opt. Phys. **50,** 133001 (2017).

[48] M. D. Lukin, M. Fleischhauer, R. Cote, L. M. Duan, D. Jaksch, J. I. Cirac, and P. Zoller, Dipole blockade and quantum information processing in mesoscopic atomic ensembles, Phys. Rev. Lett. **87,** 037901 (2001).

[49] E. Distante, A. Padrón-Brito, M. Cristiani, D. Paredes-Barato, and H. de Riedmatten, Storage enhanced nonlinearities in a cold atomic Rydberg ensemble, Phys. Rev. Lett. **117,** 113001 (2016).

[50] A. Padrón-Brito, R. Tricarico, P. Farrera, E. Distante, K. Theophilo, D. Chang, and H. de Riedmatten, Transient dynamics of the quantum light retrieved from Rydberg polaritons, New J. Phys. **23,** 063009 (2021).

[51] P. Farrera, G. Heinze, B. Albrecht, M. Ho, M. Chávez, C. Teo, N. Sangouard, and H. de Riedmatten, Generation of single photons with highly tunable wave shape from a cold atomic ensemble, Nat. Commun. **7,** 13556 (2016).

[52] A. V. Gorshkov, R. Nath, and T. Pohl, Dissipative many-body quantum optics in Rydberg media, Phys. Rev. Lett. **110,** 153601 (2013).

[53] P.-F. Sun, Y. Yu, Z.-Y. An, J. Li, C.-W. Yang, X.-H. Bao, and J.-W. Pan, Deterministic time-bin entanglement between a single photon and an atomic ensemble, Phys. Rev. Lett. **128,** 060502 (2022).

[54] G. Camy, Ch. J. Bordé, and M. Ducloy, Heterodyne saturation spectroscopy through frequency modulation of the saturating beam, Opt. Commun. **41,** 325 (1982).

[55] Y. N. M. de Escobar, S. P. Álvarez, S. Coop, T. Vanderbruggen, K. T. Kaczmarek, and M. W. Mitchell, Absolute frequency references at 1529 and 1560 nm using modulation transfer spectroscopy, Opt. Lett. **40,** 4731 (2015).

[56] R. W. P. Drever, J. L. Hall, F. V. Kowalski, J. Hough, G. M. Ford, A. J. Munley, and H. Ward, Laser phase and frequency stabilization using an optical resonator, Appl. Phys. B **31,** 97 (1983).

[57] N. Šibalić, J. D. Pritchard, C. S. Adams, and K. J. Weatherill, ARC: An open-source library for calculating properties of alkali Rydberg atoms, Comput. Phys. Commun. **220,** 319 (2017).

[58] E. Zeuthen, M. J. Gullans, M. F. Maghrebi, and A. V. Gorshkov, Correlated photon dynamics in dissipative Rydberg media, Phys. Rev. Lett. **119,** 043602 (2017).

[59] P. Bienias, J. Douglas, A. Paris-Mandoki, P. Titum, I. Mirgorodskiy, C. Tresp, E. Zeuthen, M. J. Gullans, M. Manzoni, S. Hofferberth, D. Chang, and A. V. Gorshkov, Photon propagation through dissipative Rydberg media at large input rates, Phys. Rev. Res. **2,** 033049 (2020).

[60] Which is a reasonable assumption in our case, as both of the photons are expected to be Fourier limited and their temporal modes are well matched.

[61] A. M. Brańczyk, Hong-Ou-Mandel interference, ArXiv: 1711.00080.

[62] Lowering the Rydberg state affects both the interaction strength and the coupling Rabi frequency; however, the net effect is the reduction of the blockade radius.